Accurate Characterization and Design Guidelines of Glide-Symmetric Holey EBG

Qiao Chen, *Member, IEEE*, Francisco Mesa, *Fellow, IEEE*, Xiaoxing Yin, *Member, IEEE*, and Oscar Quevedo-Teruel, *Senior Member, IEEE*

***Abstract*— The dispersion characteristics of a glide-symmetric holey periodic surface are investigated, with special emphasis on a detailed study of its stopbands. The unit cell is modeled as a multiport network associated with multiple modes at each of the lattice boundaries. Enforcing the periodic conditions, the real and imaginary parts of the wavenumbers of the Floquet modes are calculated through an eigenproblem posed in terms of the generalized multimodal transfer matrix, which is computed from the scattering parameters obtained with a full-wave simulator. This procedure allows us to take into account the higher order modal couplings between adjacent unit cells that are crucial for accurate dispersion analysis. The resulting simulation-assisted approach provides both a convenient computational tool and a very fruitful physical insight that reveals the existence of complex modes, the convergence of opposite-parity modes, and the anisotropy in both passband and stopband. This approach enables a precise calculation of the attenuation constant, which is not possible with conventional techniques as the eigenmode solvers of commercial software. Based on this approach, an extensive parametric study is carried out, rigorously establishing a set of critical criteria for the use of such a periodic surface as an electromagnetic bandgap structure in gap waveguide technology. Moreover, the analysis of the directional properties of the structure is applied to further suppress the leakage.**

***Index Terms*— Dispersion analysis, gap-waveguide, glide symmetry, metasurfaces, multimodal analysis.**

I. Introduction

A GLIDE-SYMMETRIC holey periodic surface is constructed in a narrow air gap formed by a parallel-plate waveguide (PPW), where the holes in its upper and lower metallic plates are off-shifted by half the period in both orthogonal in-plane directions. The attractive properties of such surface have driven studies on various microwave/millimeter-wave devices, including lenses [1]–[3], leaky-wave antennas [4], flanges with low leakage [5], [6], and filters [7]. In addition, these surfaces find application in gap waveguide technology as a cost-effective alternative for the electromagnetic bandgap (EBG) structures based on bed-of-nails [8], [9]. Glide-symmetric holey EBG presents a stopband whose bandwidth is substantially broader than its nonglide counterpart. This fact has been widely validated by both a theoretical analysis using a mode-matching technique [10], [11] and experimentally [12], [13]. The use of holes to replace the pins in conventional gap waveguides increases the design robustness and alleviates the manufacturing challenges, especially in mmWave bands where the tall and thin metallic pins are extremely sensitive to their details in submillimeter scale [14]. In those applications with limited space for the EBG (e.g., a phased array constrained by its element spacing), a minimum number of holes needs to be determined for a target attenuation [8], [9]. This necessarily requires the precise knowledge of the stopband characteristics, which has never been thoroughly investigated. In fact, the attenuation provided by this stopband only has been estimated from the leakage losses of a groove-gap waveguide whose lateral walls are loaded with such glide-symmetric holes [12]. To accurately characterize the structure performance, especially in its stopband a comprehensive dispersion analysis needs to be carried out.

In recent years, a lot of effort has been devoted to the proper description of a pair of periodic surfaces that are glide-symmetrically coupled to each other. As explained in [15], the complex interactions between two surfaces bring difficulties to the equivalent homogenization process that is required by the transverse-resonance method widely used in conventional metasurfaces [16], [17]. For this reason, the mode-matching technique is employed in [10], [11], and [18] for the Bloch analysis of both glide-symmetric corrugations and holey metasurfaces. This *ad hoc* method yields rigorous solutions but does not provide a direct physical interpretation. Meanwhile, an equivalent circuit approach is proposed for the 1-D glide-symmetric geometries [15], [19], [20], giving a straightforward link between their physical behaviors and the circuit topologies. The analytical nature of this equivalent-circuit method allows for highly efficient computation, but it is restricted to deal with canonical structures with circuit parameters known in closed form [21], [22].

Manuscript received April 30, 2020; revised July 4, 2020 and August 6, 2020; accepted August 25, 2020. Date of publication September 24, 2020; date of current version December 3, 2020. This work was supported in part by the Strategic Innovation Program Smarter Electronics System—A Joint Venture of Vinnova, Formas and the Swedish Energy Agency, under Project High-Int (2019-02103); in part by the Stiftelsen ÅForsk Project H-Materials under Grant 18-302; and in part by the National Natural Science Foundation of China under Grant 61771127 and Grant 61427801. The work of F. Mesa has been funded by the Spanish Government: Salvador de Madariaga fellowship PRX19/00025 and Project TEC2017-84724-P. *(Corresponding author: Qiao Chen.)*

Qiao Chen is with the Division for Electromagnetic Engineering, KTH Royal Institute of Technology, SE-100 44 Stockholm, Sweden, and also with the State Key Laboratory of Millimeter Waves, Southeast University, Nanjing 210096, China (e-mail: qiaoc@kth.se).

Francisco Mesa is with the Department of Applied Physics 1, ETS Ingeniería Informática, Universidad de Sevilla, 41004 Seville, Spain (e-mail: mesa@us.es).

Xiaoxing Yin is with the State Key Laboratory of Millimeter Waves, Southeast University, 210096 Nanjing, China (e-mail: xxyin@seu.edu.cn).

Oscar Quevedo-Teruel is with the Division for Electromagnetic Engineering, KTH Royal Institute of Technology, SE-100 44 Stockholm, Sweden (e-mail: oscarqt@kth.se).

Color versions of one or more of the figures in this article are available online at https://ieeexplore.ieee.org.

Digital Object Identifier 10.1109/TMTT.2020.3023751

In this work, a simulation-assisted generic approach [23]–[27] is applied to analyze the glide-symmetric holey metasurface, presenting excellent accuracy and a very fruitful physical insight. Similar methods have also been adopted in the analysis of conventional periodic structures [28]–[33]. Here, the dispersion analysis is carried out on a single unit cell described by a generalized multimodal transfer matrix. This matrix is converted from the simulated multimodal scattering parameters associated with multiple modes defined at each interface bounding the unit cell. By including the higher order modes, this matrix properly accounts for those couplings between adjacent unit cells that have a critical impact on the method accuracy. Because of that, some previously undetected phenomena are now found: among them, the existence of a complex mode, interchange of mode parity, and anisotropic behavior in the passbands/stopbands. This method also enables an accurate calculation of the attenuation constant in the stopband that is not possible with the eigenmode analysis of commercial software. Moreover, an exhaustive parametric analysis is performed, aimed at giving the first complete guidelines for the design of such holey metasurface as an EBG in gap waveguide technology. The knowledge of the anisotropic characteristics of the structure is used to fully exploit its stopband attenuation.

This article is organized as follows. In Section II, the multimodal characterization of the glide-symmetric holey metasurface is formulated. Then, in Section III, a careful dispersion analysis is presented, with special emphasis on the attenuation properties. In Section IV, the stopband attenuation of the glide and nonglide scenarios are compared, and the designing rules for this holey EBG are presented. Finally, the main conclusions are discussed in Section V.

II. Problem Formulation

The computation of the dispersion diagrams of periodic structures is a topic with a very long tradition in several physics and engineering areas [34]–[36]. Different semianalytical, numerical, and experimental approaches have been reported for this task (see, for instance, [22], [37]–[45]). In this section, we focus our attention on the characteristics of the Floquet modes of the glide-symmetric holey metasurface depicted in Fig. 1(a). The periodic holes drilled in the top and bottom metallic plates of the PPW are displaced against each other by half the period in both x- and y-directions.

In the framework of the network theory, a periodic structure can be modeled as an infinite cascade of the equivalent networks of its unit cells, each characterized by its transfer matrix. Imposing the Bloch condition on the cell boundaries, a dispersion analysis can be restricted to one single unit cell. As explained in [35], [46], and [47], this unit cell can be well described by a mono-modal network provided that: 1) only one Floquet mode of interest is relevant on its terminal planes bounding the cell and 2) the interactions between adjacent cells via other modes are negligible on those planes, as in the cases reported in [15] and [19]. However, these assumptions are no longer valid for the more general scenario considered

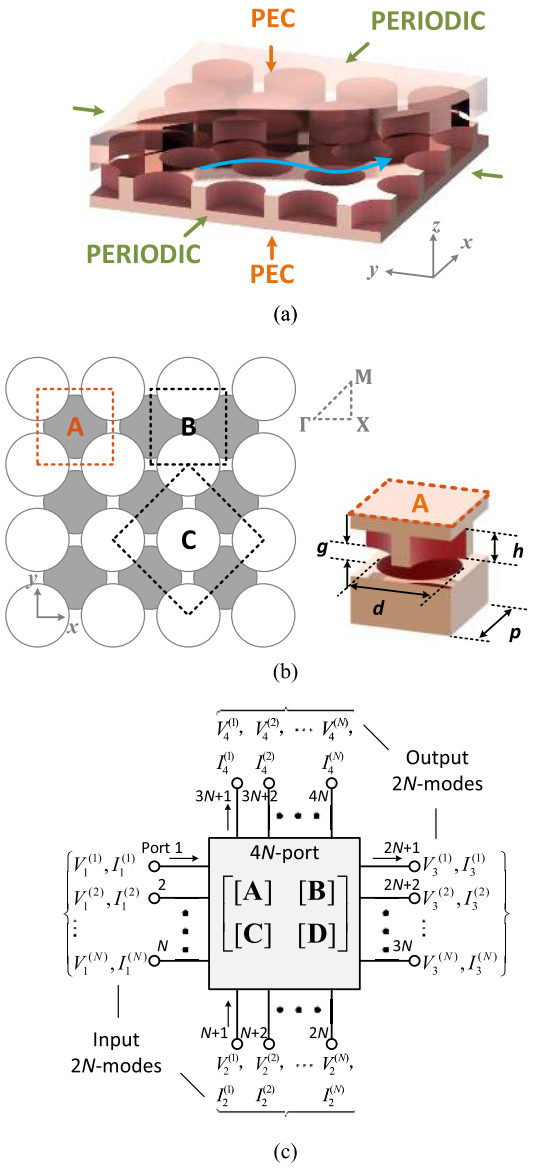

Fig. 1. Glide-symmetric holey metasurface. (a) Full structure. (b) Unit cell. The dark circles represent holes in the bottom layer and the white in the top layer. The period is denoted as p, hole diameter as d, hole depth as h, and the air gap between two layers as g. (c) Equivalent network of the unit cell characterized by a multimodal transfer matrix.

in this work. As illustrated in Fig. 1(b), in the presence of glide-symmetric holes, the unit cell boundaries are inevitably located in the holey region, through which adjacent cells are closely coupled to each other by means of evanescent-mode interactions. For this reason, the unit cell in Fig. 1(b) is modeled as a $4N$-port network with its four terminal planes placed on the side faces of the square lattice, each one related to the first N significant modes, as shown in Fig. 1(c). Considering the equivalent voltage $V_i^{(n)}$ and current $I_i^{(n)}$ associated with the nth mode at the ith terminal plane, the application of the Bloch condition to these quantities at all terminal planes gives rise to the following generalized eigenvalue problem formulated through a generalized multimodal transfer matrix

$[\mathbf{T}]_{4N\times 4N}$ [26], [27]

$$\begin{bmatrix}\mathbf{V_3}\\ \mathbf{V_4}\\ \mathbf{I_3}\\ \mathbf{I_4}\end{bmatrix} = [\mathbf{T}]_{4N\times 4N}\begin{bmatrix}\mathbf{V_1}\\ \mathbf{V_2}\\ \mathbf{I_1}\\ \mathbf{I_2}\end{bmatrix} = \begin{bmatrix}\mathrm{e}^{-\mathrm{j}k_x p}\mathbf{V_1}\\ \mathrm{e}^{-\mathrm{j}k_y p}\mathbf{V_2}\\ \mathrm{e}^{-\mathrm{j}k_x p}\mathbf{I_1}\\ \mathrm{e}^{-\mathrm{j}k_y p}\mathbf{I_2}\end{bmatrix} \tag{1}$$

where

$$\mathbf{V}_i = \left[V_i^{(1)}\ V_i^{(2)}\ \ldots\ V_i^{(N)}\right]^{\mathrm{T}}$$
$$\mathbf{I}_i = \left[I_i^{(1)}\ I_i^{(2)}\ \ldots\ I_i^{(N)}\right]^{\mathrm{T}}$$

and k_x and k_y are the modal wavenumbers in the x- and y-directions, respectively. Here, $\mathbf{V}_i, \mathbf{I}_i$ $(i = 1, 2)$ at terminal planes 1 and 2 are grouped into the effective "input" quantities and $\mathbf{V}_i, \mathbf{I}_i$ $(i = 3, 4)$ at planes 3 and 4 into the "output" quantities.

For obtaining the transfer matrix $[\mathbf{T}]$ from the multiport scattering matrix $[\mathbf{S}]$ [48], let us consider the network in Fig. 1(c), whose input ports are numbered $1, 2, \ldots, 2N$, corresponding to the $2N$ modes at terminal planes 1 and 2 and output ports $2N + 1, 2N + 2, \ldots, 4N$ corresponding to the same sets of modes at terminal planes 3 and 4. The scattering matrix of this network can be written in terms of 4 partitioned $2N \times 2N$ submatrices as

$$[\mathbf{S}] = \begin{bmatrix}[\mathbf{S}_{\mathrm{ii}}] & [\mathbf{S}_{\mathrm{io}}]\\ [\mathbf{S}_{\mathrm{oi}}] & [\mathbf{S}_{\mathrm{oo}}]\end{bmatrix} \tag{2}$$

where the subscripts i/o represent the input–output ports. If the transfer matrix $[\mathbf{T}]$ in (1) is also written in partitioned form as

$$[\mathbf{T}] = \begin{bmatrix}[\mathbf{A}] & [\mathbf{B}]\\ [\mathbf{C}] & [\mathbf{D}]\end{bmatrix} \tag{3}$$

the following explicit relations can be used:

$$[\mathbf{A}] = \frac{1}{2}[([\mathbf{I}] + [\mathbf{S}_{\mathrm{ii}}])[\mathbf{S}_{\mathrm{oi}}]^{-1}([\mathbf{I}] - [\mathbf{S}_{\mathrm{oo}}]) + [\mathbf{S}_{\mathrm{io}}]]$$
$$[\mathbf{B}] = \frac{1}{2}[([\mathbf{I}] + [\mathbf{S}_{\mathrm{ii}}])[\mathbf{S}_{\mathrm{oi}}]^{-1}([\mathbf{I}] + [\mathbf{S}_{\mathrm{oo}}]) - [\mathbf{S}_{\mathrm{io}}]][\mathbf{Z}_{\mathrm{o}}]$$
$$[\mathbf{C}] = \frac{1}{2}[\mathbf{Z}_{\mathrm{i}}]^{-1}[([\mathbf{I}] - [\mathbf{S}_{\mathrm{ii}}])[\mathbf{S}_{\mathrm{oi}}]^{-1}([\mathbf{I}] - [\mathbf{S}_{\mathrm{oo}}]) - [\mathbf{S}_{\mathrm{io}}]]$$
$$[\mathbf{D}] = \frac{1}{2}[\mathbf{Z}_{\mathrm{i}}]^{-1}[([\mathbf{I}] - [\mathbf{S}_{\mathrm{ii}}])[\mathbf{S}_{\mathrm{oi}}]^{-1}([\mathbf{I}] + [\mathbf{S}_{\mathrm{oo}}]) + [\mathbf{S}_{\mathrm{io}}]][\mathbf{Z}_{\mathrm{o}}]$$

with $[\mathbf{I}]_{2N\times 2N}$ being the identity matrix and $[\mathbf{Z}_{\mathrm{i}}]_{2N\times 2N}$ and $[\mathbf{Z}_{\mathrm{o}}]_{2N\times 2N}$ diagonal matrices whose entries are the characteristic port impedances. It should be noted that the specific value of each port impedance does not affect the eigenvalues of $[\mathbf{T}]$ as long as that impedance value is the same for the same mode at both input and output ports [27], namely, as long as

$$[\mathbf{Z}_{\mathrm{i}}] = [\mathbf{Z}_{\mathrm{o}}]. \tag{4}$$

The sets of (k_x, k_y) that satisfy (1) can be calculated on the Brillouin zone edge of the complex $\mathbf{k}$ space by solving the following dispersion equation as a function of frequency f:

$$D(k_x, k_y, f) = \det\{[\mathbf{T}(f)] - [\mathbf{\Lambda}(k_x, k_y)]\} = 0 \tag{5}$$

where $[\mathbf{\Lambda}]_{4N\times 4N}$ is a square diagonal matrix whose elements along the main diagonal are given by the row vector $[(\mathrm{e}^{-\mathrm{j}k_x p})_{1\times N}, (\mathrm{e}^{-\mathrm{j}k_y p})_{1\times N}, (\mathrm{e}^{-\mathrm{j}k_x p})_{1\times N}, (\mathrm{e}^{-\mathrm{j}k_y p})_{1\times N}]$. It is worth noting here that, in the general case of N modes, the characteristic equation defined in (5) gives rise to a $2N$-degree polynomial of two variables ($\lambda_x = \mathrm{e}^{-\mathrm{j}k_x p}$ and $\lambda_y = \mathrm{e}^{-\mathrm{j}k_y p}$). Since there is not an easy systematic way of obtaining the frequency-dependent coefficients of this characteristic polynomial, the suggested simple and general way to solve for the $2N$ roots of the polynomial equation is to fix the frequency and use a zero-searching algorithm to locate the complex zeros of the resulting determinant $D_f(k_x, k_y)$. Provided that the structure under study is reciprocal, the $2N$ roots of $D_f(k_x, k_y)$ should correspond to pairs of plus/minus N modal wavenumber solutions $(\pm k_x, \pm k_y)$. Fortunately, the absence of poles and/or branch singularities in $D_f(k_x, k_y)$ simplifies considerably the numerical task of searching for the complex zeros. An additional interesting feature of (5) is that, once the frequency is fixed, the computational cost of constructing $D_f(k_x, k_y)$ is very reduced since only matrix $[\mathbf{\Lambda}]$ needs to be updated in the searching procedure.

III. Multimodal Bloch Analysis

A proper geometrical definition of the unit cell is crucial in the multimodal analysis for two reasons. First, it should be considered that the field pattern of the Floquet modes in the unit cell has a nonnegligible projection (reaction) onto the modes of the corresponding waveguides at the input–output ports. Thus, to ensure the accuracy of the method, a very convenient practical rule is to maximize the open area on the boundaries so that all relevant modal fields can be suited. For instance, the interfaces of a nonglide holey unit cell are preferably selected in the middle of the holes (as it will be the case in Fig. 8 (inset) within the red frame). In contrast, a nonglide unit cell that enclosed the complete hole would lead to boundaries coinciding with the narrow slit of the unperturbed PPW, geometry where the required higher order modes could hardly settle themselves down. For the glide holey unit cell, a convenient choice is the one shown in the inset of Fig. 2(b). Second, the overall operational procedure of the multimodal approach is greatly simplified by choosing a centrally-symmetric unit cell that satisfies (4). Note that this condition does not require the presence of geometrical symmetries in the unit cell itself although the presence of such symmetries could be advantageously used for the computation of the required scattering matrix. Instead, condition (4) only requires the existence of symmetry of the unit-cell boundaries on account of the fact that the characteristic port impedance for each mode only depends on the physical shape of that port. For these reasons, the two most convenient choices in the glide periodic configuration in Fig. 1(a) are unit cells A and B shown in Fig. 1(b). In the following analysis, unit cell A is employed although unit cell B yields the same results.

The multimodal scattering parameters of the unit cell shown in the inset of Fig. 2(b) were simulated by CST frequency-domain solver (FDS), with hexahedral meshing and open boundaries set on the four physical ports at the side faces

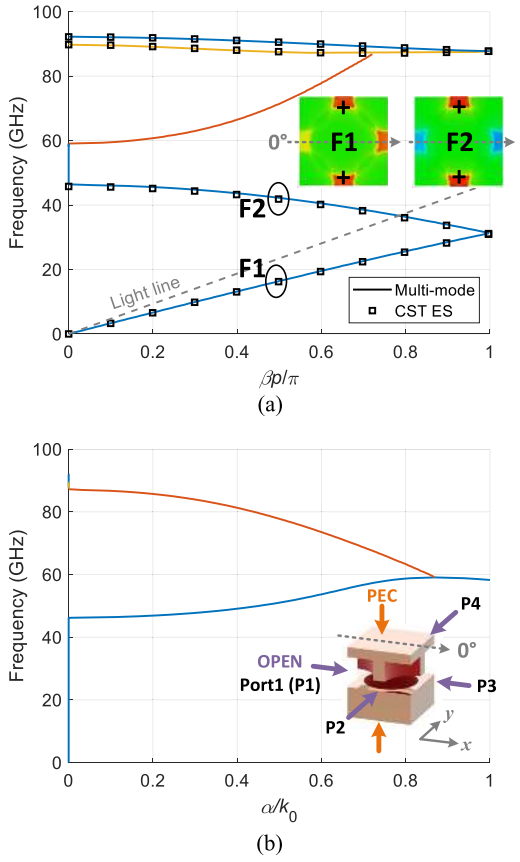

Fig. 2. Bloch analysis in the first Brillouin zone $\overline{\Gamma X}$ (0°-direction measured from the x-axis). (a) Phase shift ($\beta p/\pi$), with the insets depicting the distribution of E_z-component obtained with CST ES. (b) Normalized attenuation constant (α/k_0), with the inset showing the setups in CST FDS. The dimensions as denoted in Fig. 1(b) are $p = 3.2$ mm, $d = 0.8p = 2.56$ mm, $h = 0.31p = 1$ mm, and $g = 50$ μm. These dimensions apply throughout this article, unless otherwise specified.

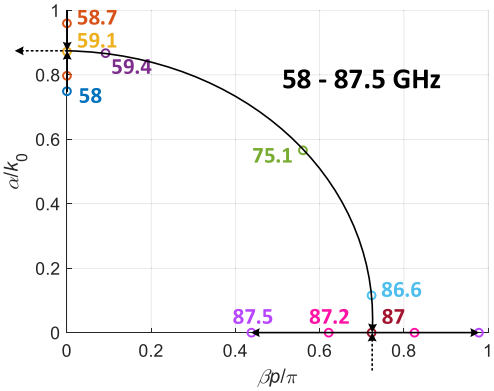

Fig. 3. Root loci of the modes presented in Fig. 2 from 58 to 87.5 GHz in the domain of $0 \le \beta \le \pi/p$, $0 \le \alpha \le k_0$. The zeros at the sampled frequencies are distinguished by the colored markers, and those at the same frequency are marked with the same color. The dashed arrow lines represent the image results that always appear in pairs and, thus, are omitted for simplicity.

of the cell, each excited by N modes. Applying (3)–(5) for $k_y = 0$ and $k_x = \beta - \mathrm{j}\alpha$ in the range of $0 \le \beta \le \pi/p$, $0 \le \alpha \le k_0$, we obtain simultaneously β and α in the first Brillouin zone $\overline{\Gamma X}$ (or 0°-direction measured along the x-axis), as shown in Fig. 2. Here, a good numerical convergence of the multimodal approach is achieved by taking $N = 5$ modes at each physical port. It should be mentioned that although a waveguide-port higher order mode excited below its cutoff frequency is evanescent, its modal fields can be required for describing the global propagation and attenuation properties; fact that has also been validated in [26] and [27]. As shown in Fig. 2(a), a good agreement is achieved in β between the results obtained with the multimodal approach and CST eigenmode solver (ES), whereas α in Fig. 2(b) cannot be compared due to the lack of results for this parameter from the ES in CST. The two lowest order modes [highlighted in blue color in Fig. 2(a)] are actually two branches of the same mode. This assertion is validated by the application of the "correlation method" reported in [49] and also employed, for instance, in [23], [24]. The perfect correlation found between the modes of these two branches is also corroborated by the fact that they have similar modal fields, as exemplified in the plots of their E_z-component at frequencies 1 and 2 (denoted by F1 and F2) given in the insets of Fig. 2(a).

An interesting consequence of performing the zero searching of (5) in the complex plane is the appearance of a previously unnoticed complex mode (highlighted in red), which appears from 59 to 87 GHz within the stopband (mode that cannot be captured by CST-ES which only calculates real modes). Remarkably, the dispersion curve corresponding to this mode does not reach $\beta p/\pi = 1$ but rather splits into two modes (represented by the yellow line) at around 87 GHz. For a better understanding of this modal transition, Fig. 3 shows the locus in the complex plane of the wavenumber ($k_x = \beta - \mathrm{j}\alpha$) as a function of frequency. An important fact to consider here is that any of the possible solutions (k_x, k_y) of the characteristic polynomial equation (5) is a continuous function of frequency. It means that the N pairs of solutions of (5) have to show continuous behavior when plotted versus frequency. Consequently, the modal solutions can neither appear nor disappear as frequency varies; instead, they can only transition from one type of mode to another. For the present nonradiative lossless structure under study, this well-known observation [35], [50] implies that modes can transition from propagative to either evanescent or complex, and vice versa.

The abovementioned transitions can be observed in Fig. 3, which shows the evolution of the relevant modes in the range of 59–87 GHz. Below 58 GHz, corresponding to the blue curves in Fig. 2, it can be observed that the mode is propagative at low frequencies and then transitions into an evanescent mode at ~46 GHz. As frequency increases, another evanescent mode appears with high values of α. Fig. 3 shows that this mode moves toward the previous evanescent mode along the imaginary axis, and they meet together at ~59.1 GHz to transition into a pair of complex modes with positive/negative phase constant ($\pm\beta - \mathrm{j}\alpha$). This type of transition has already been reported in the literature for other simpler nonperiodic and periodic structures [29], [50]–[54], and it is expected to occur in any periodic structure although its study in geometrically complex periodic structures would

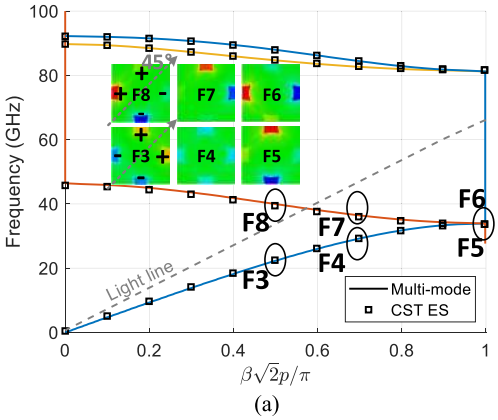

(a)

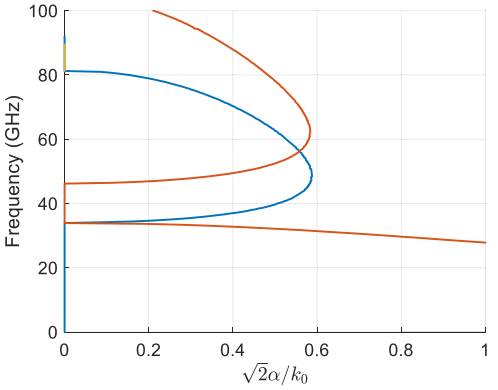

(b)

Fig. 4. Bloch analysis in the third Brillouin zone $\overline{\Gamma M}$ (45°-direction measured from the x-axis). (a) β, with the insets depicting the distribution of E_z-component obtained with CST ES. (b) α. β has been renormalized to $\sqrt{2}p$, and α has been rescaled by $\sqrt{2}$. The setups in CST FDS and dimensions are the same as in Fig. 2.

require the use of advanced simulation-assisted approaches as the one reported in this work.

The role of complex modes in bounded structures was the object of intense research a few decades ago [50]–[53], [55], and it was concluded that, in reciprocal structures, these modes are always excited in pairs giving rise to a sort of "modulated" evanescent mode [50], [53]. The complex mode in Fig. 2 is then the consequence of a common modal transition that ensures the continuity of the modal wavenumbers with respect to frequency, as illustrated in Fig. 3. The locus of this complex mode can be seen to evolve with frequency until it reaches the real axis of the complex plane at around 87 GHz, where it meets another complex mode, and this pair now transitions to another pair of propagative real modes [highlighted in yellow in Fig. 2(a)].

A similar procedure, letting $k_y = k_x \equiv k$ and solving (5) for k in the domain of $0 \leq \beta p/\pi \leq 1$, $0 \leq \alpha/k_0 \leq 1$, yields the results in the third Brillouin zone $\overline{\Gamma M}$ shown in Fig. 4. Same as in Fig. 2, numerical convergence of the multimodal approach occurs again by taking $N = 5$ modes at each excitation port. Since k stands here for either the x- or y-component of the wave vector in the 45°-direction, this vector can be written as $\mathbf{k}_{xy} = k(\hat{\boldsymbol{x}} + \hat{\boldsymbol{y}})$, with $|\mathbf{k}_{xy}| = \sqrt{2}k$. In fact, the same results for $k = \beta - \mathrm{j}\alpha$ are found when using

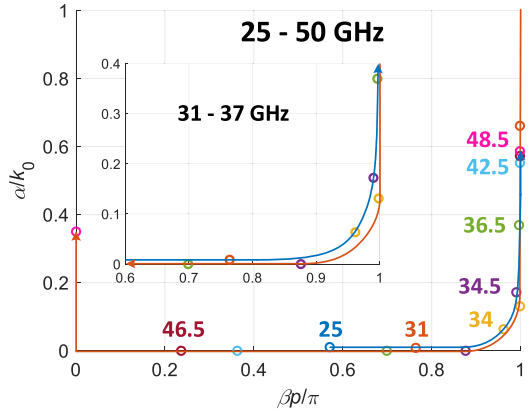

Fig. 5. Root loci of the modes reported in Fig. 4 from 25 to 50 GHz. The zeros at sampled frequencies are distinguished by colored markers, and those at the same frequency have the same color. The solid blue and red arrow lines represent the even- and odd-parity modes in Fig. 4, respectively. A small dissipation loss of $\sigma = 0.0277$ S/m is employed in simulations to avoid overlapping of the loci of these two modes.

unit cell A along the 45°-direction and with unit cell C [defined in Fig. 1(b)] in the same direction.

In contrast with the discussion for the 0°-direction case in Fig. 2, the dispersion diagrams in Fig. 4 seem to indicate that now there are two modes of different nature at low frequencies: one real propagative ($k = \beta - \mathrm{j}0$: blue line) and another evanescent ($k = \sqrt{2}\pi/p - \mathrm{j}\alpha$: red line). These two modes appear to meet together at around 34 GHz, where they transition into an evanescent mode and a propagative mode, respectively. The first hint that the transition occurs in this way (rather than the two propagative modes being just two branches of the same mode) is given by the E_z-field patterns shown in the insets of Fig. 4(a). It can be observed that the E-field pattern of the first mode exemplified at frequency F3 is evenly distributed with respect to the 45°-direction, whereas the pattern of the second mode at F8 is oddly distributed. The evolution from one pattern to another can be appreciated in the insets of Fig. 4(a). In particular, it is interesting to note the strong difference between the patterns at F5 and F6, which is in complete correspondence with the results computed by the application of the "correlation method" [24], [49]; namely, the correlation between the modal eigenvectors associated with F5 and F6 modal solutions is practically zero. Interestingly, the abovementioned modal transition finds some similarities with the appearance of Dirac points reported in 2-D photonic crystals [56].

Additional verification of this modal differentiation is provided in Fig. 5, which shows the frequency evolution of the complex wavenumbers of these two modes in the range 25–50 GHz. In similarity with the analysis carried out in [54], a low level of losses is assumed in the free space [relative permittivity given by $\varepsilon_r = 1 - \mathrm{j}\sigma/(\omega\varepsilon_0)$] to avoid that the loci of the modes overlap. Different locus trajectories of the modes plotted in Fig. 5 clearly show that these two modes are independent solutions that turn out to have very similar numerical values at ~34 GHz. As $\sigma \to 0$, the modal trajectories run along the horizontal and vertical axes, making it very difficult to determine whether the modal continuation

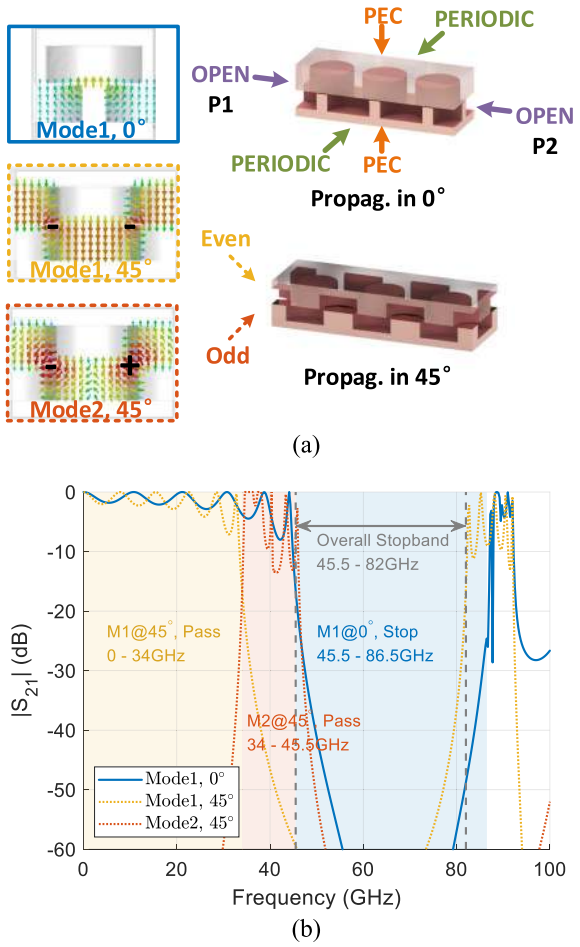

Fig. 6. Analysis of scattering characteristics in the first Brillouin zone $\overline{\Gamma X}$ (0°-direction) and third Brillouin zone $\overline{\Gamma M}$ (45°-direction) using CST FDS. (a) Excited modes at the ports and solving setups for both directions. The unit cells A and C in Fig. 1(b) are employed for the 0°- and 45°-directions, respectively. (b) Scattering parameters of the excited modes in both directions. The dimensions are the same as in Fig. 2.

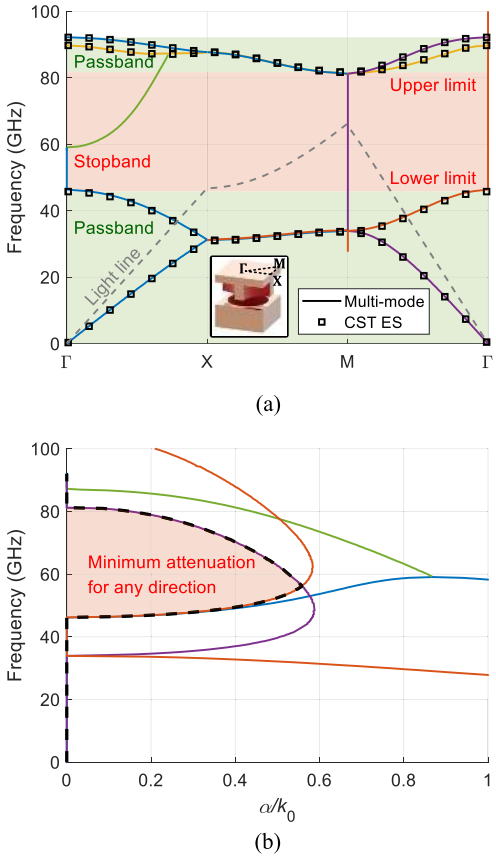

Fig. 7. (a) Full dispersion diagram of the Billouin zone $\overline{\Gamma XM\Gamma}$ and the total stopband shaded in red. (b) Attenuation curves of the Billouin zone $\overline{\Gamma X}$ and $\overline{M\Gamma}$ and minimum attenuation for any direction enveloped by the black dashed line corresponding to the total stopband. The modes are distinguished by different colors, and the dimensions are the same as in Fig. 2.

happens as already discussed or as the one found for the 0°-direction case.

In order to gain a deeper physical insight on the relevant consequences of the directional properties of the present structure (namely, observed anisotropy in the 0°- and 45°-directions), Fig. 6(b) shows the magnitude of the transmission scattering parameters associated with the relevant modes discussed earlier. The appearance of these directional properties was also reported in the study of orthotropic waveguides [57] and photonic/phononic crystals [56], [58]–[60]. In our case, the S_{21} parameter is computed through CST FDS by using a hexahedral meshing to simulate the two finite-periodic configurations shown in Fig. 6(a). Specifically, a repetition of three unit cells A and C in Fig. 1(b) is employed to analyze the propagation along the 0°- and 45°-directions, respectively (periodic conditions are imposed in the transverse direction). The blue solid line in Fig. 6(b) clearly shows that the first passband of the so-called "Mode1, 0°" (directional passband along the 0°-direction) ends at 45.5 GHz. This result agrees with our previous assumption that the two lowest order modes in Fig. 2(a) were two branches of the same physical mode; additionally corroborated by the fact that they have a similar modal pattern, the projection of which at the input port is exemplified in the blue-framed picture in Fig. 6(a). Also, the location of the second passband of this mode in Fig. 6(b) coincides with the second passband of the mode highlighted in blue color at the top of Fig. 2. In the 45°-direction, the transmission coefficient of the even mode (denoted as "Mode1, 45°" and plotted with yellow dotted line) shows a stopband that starts from 34 GHz, and the other mode with odd parity ("Mode2, 45°", plotted with red dotted line) shows a directional passband also starting at 34 GHz and ending at $\sim$ 45.5 GHz. This fact supports our previous discussion about the different nature of these modes in Fig. 4 and that the wavenumber loci of these opposite-parity modes meet at 34 GHz. The results in Fig. 6(b) can be seen to match the complete Brillouin diagram shown in Fig. 7 for both the phase and attenuation constants.

The abovementioned discussion about the directional passband and stopband properties shown in Fig. 6(b) can bring some important practical consequences. Commonly, the total (omnidirectional) stopband of a periodic structure is defined as the region where there are not propagative modes. However, we have shown that there exists a partial (directional) stopband bandwidth for even- and odd-parity modes. This fact can be

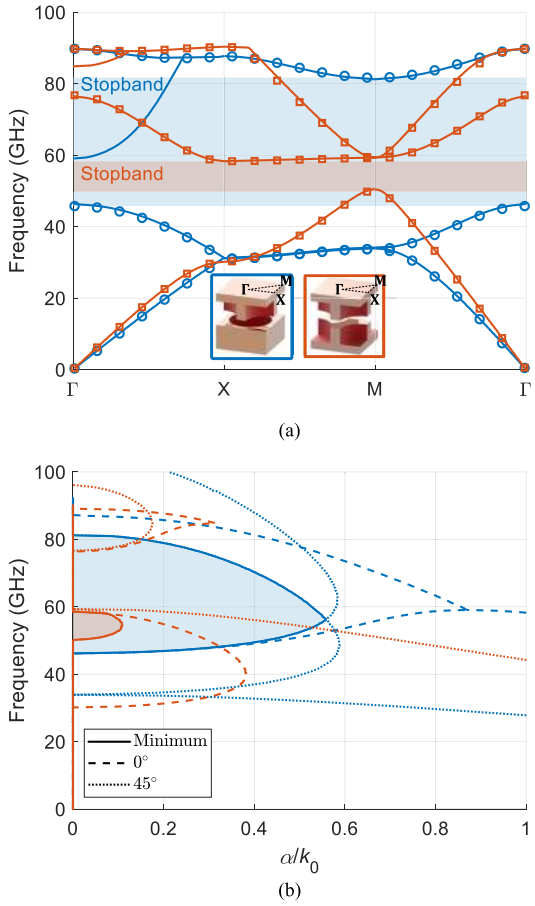

Fig. 8. Comparison of the stopband of glide- and nonglide scenarios. (a) Full dispersion diagram of the Brillouin zone $\overline{\Gamma XM\Gamma}$ with the overall stopband shaded in colors. The data points on the Brillouin zone boundaries (namely $\beta = n\pi/p, n = 0, 1, 2, 3$) are omitted for simplicity. (b) Attenuation at $\overline{\Gamma X}$ (0°) and $\overline{M\Gamma}$ (45°) and the minimum attenuation for any direction. The results obtained with the multimodal method are represented by lines, and those with CST ES are represented by markers in the corresponding colors. The dimensions of the two unit cells are the same as in Fig. 2.

advantageously used for a given practical configuration in which the designer knows a priory nature (i.e., the parity) of the arriving waves, in similarity with the application of these directional properties to the design of an acoustic frequency filter reported in [60]. In Section IV-C, we demonstrate how to employ the knowledge of the directional properties of the stopband to enhance the suppression of the leakage from a glide-symmetric holey groove gap waveguide.

IV. Design Guidelines

A. Glide Symmetry

The analysis of Section III demonstrates the existence of multiple modes that present directional properties in the frequency band of interest. For better reference and comparison of the stopband in the following studies, only the minimum attenuation for any direction provided by the total stopband will be examined (for instance, the one shaded in red color in Fig. 7).

In Fig. 8, the stopband performance of the glide and nonglide configurations are compared. The nonglide case is analyzed following the same procedure as the one for its glide counterpart introduced in Section III, except that only $N = 3$ modes at each port is required to achieve convergence in this nonglide case, instead of $N = 5$ needed for the glide scenario. This difference evidences the existence of more complex higher order interactions in the glide-symmetric case, which shows a wider stopband and higher attenuation levels in these bands (the rejection within the stopband is stronger). Similar to the glide configuration, the existence and transition of a complex mode are detected from 84.9 to 88.9 GHz in the first Brillouin zone $\overline{\Gamma X}$ of the nonglide case. The opposite-parity modes are also found in the 45°-direction. Other than that, these two cases exhibit very different behaviors in their respective stopbands and passbands. The degenerate lowest order modes in the 0°-direction are found to exist only in the presence of glide symmetry. Moreover, the glide topology provides a higher value of attenuation than its nonglide counterpart in the 0°-direction. This difference is even more prominent in the 45°-direction, where both bandwidth and attenuation of the stopband in the nonglide case are severely limited by the proximity of its first and second passbands, restricting the stopband for any direction. For these reasons, the glide configuration is a superior solution for the EBG applications compared with its nonglide version [5], [12], [13].

B. Optimal Dimensions

Extensive parametric studies on the stopband behaviors of the glide-symmetric holey EBG have been carried out, some of these results being shown in Fig. 9. As revealed in Fig. 9(a), the stopband range always increases by decreasing the unwanted air gap g. Taking the case of $d/p = 0.8$ in Fig. 9(a) as an example, the smaller value of g also improves the stopband attenuation, as evidenced in Fig. 9(d). In general, the smaller the gap, the better the performance of the stopband. In practice, the upper and lower metallic plates are tightly fastened by screws to ensure a close contact, leaving a gap typically no larger than 50 μm, as assumed in [4] and [14]. Thus, $g = 50$ μm will be considered the worst case scenario for the following studies. Aimed at maximizing the attenuation in a stopband centered around 60 GHz, Fig. 9(b) and (e) shows that the optimum diameter of the holes is found around $d = 0.8p$, which yields a bandwidth of 57 % and a minimum normalized attenuation of 0.52 for any direction at 60 GHz; α/k_0 reaches 0.85 in the 0°-direction at the same frequency. Therefore, it is crucial to ensure this optimum radio of d/p since any value deviated from the optimum one results in a rapid deterioration of the stopband. In addition, Fig. 9(c) and (f) shows that the hole depth has a minor impact on the stopband as long as $h > 1$ mm ($0.31p$). The insensitivity of this parameter suggests that more cost-effective manufacturing can be facilitated by simply drilling or molding rather than milling, as usually done for the conventional bed-of-nails structures, given that the hole allows for more tolerances in its bottom.

Based on the previous study, the following guidelines can be used to enhance the design of the present glide-symmetric holey EBG. First, the maximum air gap in the EBG region needs to be estimated as a design reference according to

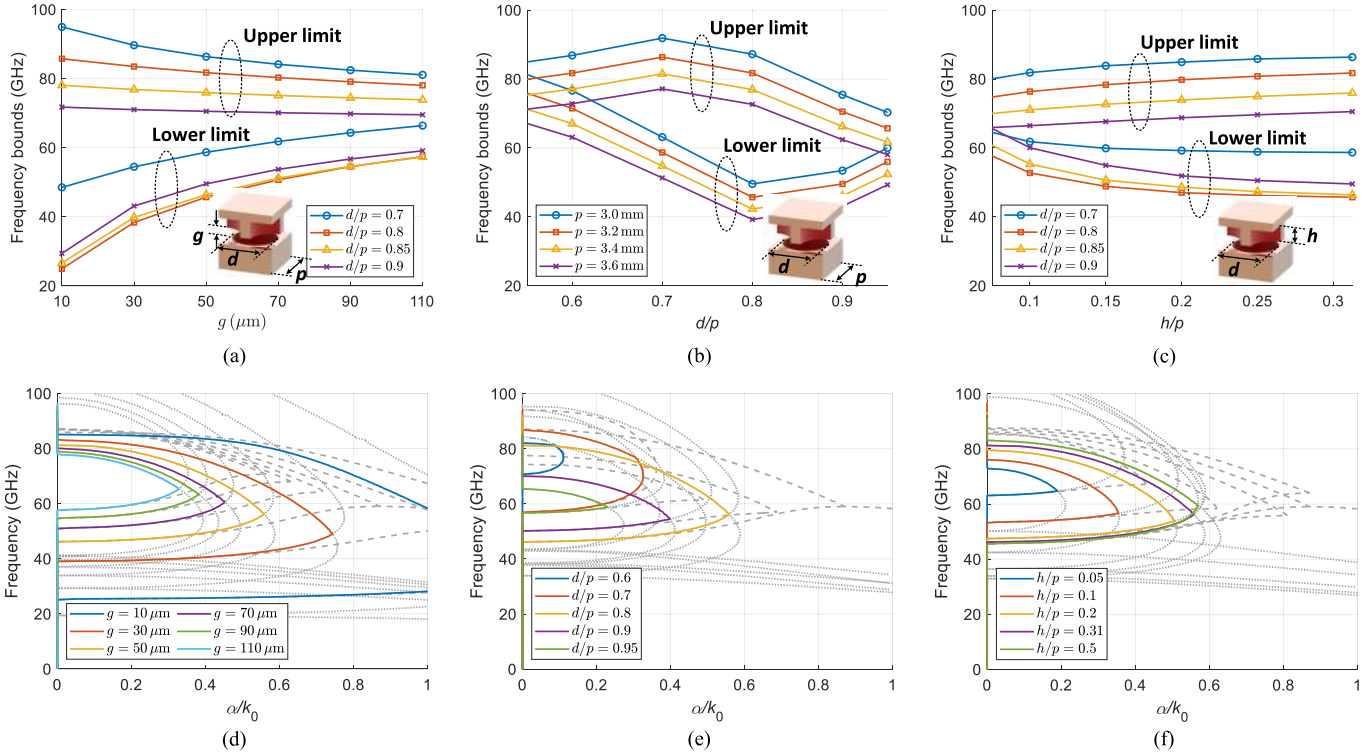

Fig. 9. Parametric study of stopband characteristics. (a)–(c) Frequency bounds of the overall stopband as a function of the swept geometrical parameters. (d)–(f) Attenuation as a function of the same set of parameters in the 0°- and 45°-directions represented by the gray dashed lines and dotted lines, respectively, and the minimum attenuation for any direction provided by the stopband outlined by the colored solid lines. In all cases, the dimensions are $p = 3.2$ mm, $d/p = 0.8$, $h = 1$ mm, and $g = 50$ μm, unless otherwise specified.

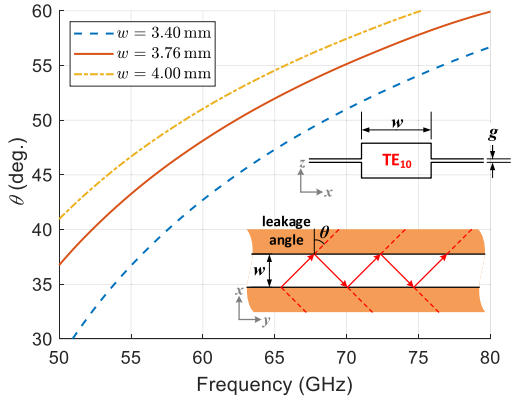

Fig. 10. Leakage direction of the fundamental TE_{10} mode of a rectangular waveguide with a narrow slit of $g = 50$ μm. The leakage angle is calculated by $\theta = \arcsin \beta/k_0$, with β being the phase constant of the quasi-TE_{10} mode and k_0 the free-space wavenumber (same as in the PPW region).

the deformation constraints in the manufacturing process. In general, $g < 50$ μm can be assumed, and $g = 10$ μm for the deployment in small areas (good contact is, thus, ensured). Then, a proper period p can be set to locate the stopband in the band of interest. Next, letting $d \approx 0.8p$ and $h > 0.3p$ ensures the optimum bandwidth and attenuation. Finally, the number of unit cells required to achieve the target suppression has to be selected by referring to the data given in Fig. 9(d)–(f).

C. Arrangement of Holes

Once the optimal dimensions of the holey EBG unit cells are determined, a practical case is now considered where the holes are employed in the slit of a groove gap waveguide to suppress the leakage from the guiding structure. Gap waveguide technology is ideal for millimeter-wave applications where substrate integrated waveguides have elevated losses due to the propagation in a dielectric material [61]. In some cases, the use of glide-symmetric holes is more cost-effective than pin-type periodic structures [13].

In groove gap waveguides (with TE_{10} mode), the leakage comes from the imperfect reflection of the impinging constituent waves of wave vectors $\mathbf{k} = \pm(\pi/w)\hat{\mathbf{x}} + \beta\hat{\mathbf{y}}$ on the lateral walls of the channel, which occurs at an angle $\theta = \arcsin(\beta/k_0)$, as illustrated in the inset of Fig. 10. Depending on the arrangement of the holes embedded in the upper/lower walls of the slit region, the leaked waves can undergo different directional stopbands due to the anisotropy of the holey EBG unit cell and, thus, experience different attenuation rates. In Fig. 11, two configurations are compared when the glide-symmetric holey EBG is excited with different incidence angles by the TE_{10} mode of a rectangular waveguide. This type of analysis, based on field attenuation, has also been employed in the studies on other gap waveguides [13], [61]. The unit cells are arranged in such a manner that their 0°/ 45°-direction roughly aligns with the leakage direction at 60 GHz in Fig. 11(a)/(b). Since, in the considered frequency range, a higher value of α is found in the 0°-direction than in the 45°-direction (only the even mode of the holey EBG should be considered), a higher attenuation rate is achieved in the case of Fig. 11(a). To properly evaluate the attenuation rate, one has to refer to the maximum levels of the electric

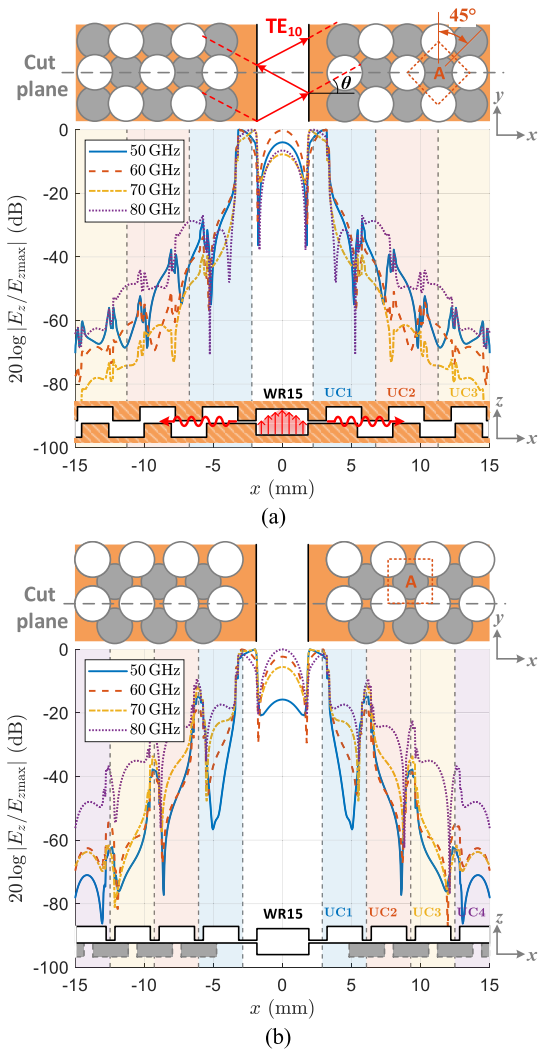

Fig. 11. Suppression rate of the leaked electric fields in glide-symmetric holey groove waveguides, whose lateral walls are loaded with the holey unit cells [see Fig. 1(b)] rotated by (a) 45° and (b) 0°. Same as indicated in Fig. 1, the dark circles represent holes in the bottom layer and the white in the top, with the same dimensions as in Fig. 2. The guiding channel replicates a WR15 rectangular waveguide (width 3.76 mm and height 1.88 mm) with a slit of 50 μm. The electric fields are simulated by the CST time-domain solver.

field, which fluctuates periodically between holes and parallel plate regions. At 60 GHz, for instance, the attenuation level is suppressed below -30 dB beyond two rows of holes in Fig. 11(b), while this level is further attenuated below -50 dB in Fig. 11(a). Also, the attenuation rate at 80 GHz in Fig. 11(b) is severely deteriorated in comparison with that of Fig. 11(a), given the fact that the value of α provided by the even mode of the unit cell is quite small [see Fig. 7(b) (purple line)].

The significant difference in the attenuation rates between the two cases analyzed in Fig. 11 was somewhat expected at the light of the results shown in Fig. 9. For instance, in the worst case scenario with $g = 50$ μm, it can be observed in that figure that $\alpha/k_0 = 0.52$ at 60 GHz, which means that two rows of glide-symmetric holes should offer a total stopband attenuation given by $e^{-2\alpha \cdot 2p} = -36$ dB, in good correspondence with the data in Fig. 11(b). Since the attenuation constant in the 0°-direction increases up to $\alpha/k_0 = 0.85$ at 60 GHz, giving rise to an attenuation level of $e^{-2\alpha \cdot 2p} = -59$ dB, particular advice for gap waveguide applications is to arrange the holey unit cells so that their 0°-direction aligns with the direction of the impinging waves. This arrangement also minimizes the reflections from the EBG by avoiding a saw-toothed interface between the EBG and lateral wall of the waveguide groove [see Fig. 11 (insets)], as mentioned in [4] and [13].

V. Conclusion

In this work, a multimodal transfer matrix approach is employed in the Bloch analysis of the dispersion diagrams of a glide-symmetric holey metasurface. Glide symmetries were demonstrated to be able to reduce the dispersion of conventional periodic structures [1] and widen the bandwidth of EBGs [12]. The proposed approach in this article is able to calculate both the phase and attenuation constants of the modal wavenumbers of the structure. In particular, a precise calculation of the attenuation constant is not possible with conventional techniques, as the CST eigenmode solver. Here, we accurately characterized the attenuation properties of glide-symmetric EBGs, which is essential for the design of flanges with reduced leakage [5], [6], filters [7], or gap waveguide technology [13].

The proposed approach has also made possible the finding of some relevant interesting phenomena, including the existence of complex modes, mode conversion, the convergence of the even- and odd-parity modes, and the directional properties in both passband and stopband. Based on an exhaustive parametric study of the stopband properties using the present multimodal approach, a complete set of criteria can be set up for the use of a glide-symmetric metasurface as an EBG in gap waveguide technology. Moreover, as a practical example, we show that the knowledge of the directional properties of the holey metasurface can be advantageously used to enhance its stopband attenuation.

References

[1] O. Quevedo-Teruel, M. Ebrahimpouri, and M. N. M. Kehn, "Ultrawideband metasurface lenses based on off-shifted opposite layers," *IEEE Antennas Wireless Propag. Lett.*, vol. 15, pp. 484–487, Dec. 2016.

[2] O. Quevedo-Teruel, J. Miao, M. Mattsson, A. Algaba-Brazalez, M. Johansson, and L. Manholm, "Glide-symmetric fully metallic luneburg lens for 5G communications at ka-band," *IEEE Antennas Wireless Propag. Lett.*, vol. 17, no. 9, pp. 1588–1592, Sep. 2018.

[3] P. Bantavis, C. G. Gonzalez, R. Sauleau, G. Goussetis, S. Tubau, and H. Legay, "Broadband graded index gutman lens with a wide field of view utilizing artificial dielectrics: A design methodology," *Opt. Express*, vol. 28, no. 10, pp. 14648–14661, May 2020.

[4] Q. Chen, O. Zetterstrom, E. Pucci, A. Palomares-Caballero, P. Padilla, and O. Quevedo-Teruel, "Glide-symmetric holey leaky-wave antenna with low dispersion for 60 GHz point-to-point communications," *IEEE Trans. Antennas Propag.*, vol. 68, no. 3, pp. 1925–1936, Mar. 2020.

[5] M. Ebrahimpouri, A. A. Brazalez, L. Manholm, and O. Quevedo-Teruel, "Using glide-symmetric holes to reduce leakage between waveguide flanges," *IEEE Microw. Wireless Compon. Lett.*, vol. 28, no. 6, pp. 473–475, Jun. 2018.

[6] Z. He, S. An, J. Liu, and C. Jin, "Variable high precision wide D-band phase shifter," *IEEE Access*, vol. 8, pp. 140438–140444, 2020.

[7] A. Monje-Real, N. J. G. Fonseca, O. Zetterstrom, E. Pucci, and O. Quevedo-Teruel, "Holey glide-symmetric filters for 5G at millimeter-wave frequencies," *IEEE Microw. Wireless Compon. Lett.*, vol. 30, no. 1, pp. 31–34, Jan. 2020.

[8] E. Rajo-Iglesias, M. Ebrahimpouri, and O. Quevedo-Teruel, "Wideband phase shifter in groove gap waveguide technology implemented with glide-symmetric holey EBG," *IEEE Microw. Wireless Compon. Lett.*, vol. 28, no. 6, pp. 476–478, Jun. 2018.

[9] Q. Liao, E. Rajo-Iglesias, and O. Quevedo-Teruel, "*Ka*-band fully metallic TE40 slot array antenna with glide-symmetric gap waveguide technology," *IEEE Trans. Antennas Propag.*, vol. 67, no. 10, pp. 6410–6418, Oct. 2019.

[10] F. Ghasemifard, M. Norgren, O. Quevedo-Teruel, and G. Valerio, "Analyzing glide-symmetric holey metasurfaces using a generalized Floquet theorem," *IEEE Access*, vol. 6, pp. 71743–71750, Nov. 2018.

[11] G. Valerio, F. Ghasemifard, Z. Sipus, and O. Quevedo-Teruel, "Glide-symmetric all-metal holey metasurfaces for low-dispersive artificial materials: Modeling and properties," *IEEE Trans. Microw. Theory Techn.*, vol. 66, no. 7, pp. 3210–3223, Jul. 2018.

[12] M. Ebrahimpouri, O. Quevedo-Teruel, and E. Rajo-Iglesias, "Design guidelines for gap waveguide technology based on glide-symmetric holey structures," *IEEE Microw. Wireless Compon. Lett.*, vol. 27, no. 6, pp. 542–544, Jun. 2017.

[13] M. Ebrahimpouri, E. Rajo-Iglesias, Z. Sipus, and O. Quevedo-Teruel, "Cost-effective gap waveguide technology based on glide-symmetric holey EBG structures," *IEEE Trans. Microw. Theory Techn.*, vol. 66, no. 2, pp. 927–934, Feb. 2018.

[14] O. Zetterstrom, E. Pucci, P. Padilla, L. Wang, and O. Quevedo-Teruel, "Low-dispersive leaky-wave antennas for mmWave point-to-point high-throughput communications," *IEEE Trans. Antennas Propag.*, vol. 68, no. 3, pp. 1322–1331, Mar. 2020.

[15] G. Valerio, Z. Sipus, A. Grbic, and O. Quevedo-Teruel, "Accurate equivalent-circuit descriptions of thin glide-symmetric corrugated metasurfaces," *IEEE Trans. Antennas Propag.*, vol. 65, no. 5, pp. 2695–2700, May 2017.

[16] M. Bosiljevac, Z. Sipus, and P. S. Kildal, "Construction of Green's functions of parallel plates with periodic texture with application to gap waveguides—A plane-wave spectral-domain approach," *IET Microw., Antennas Propag.*, vol. 4, no. 11, pp. 1799–1810, Nov. 2010.

[17] G. Valerio, D. R. Jackson, and A. Galli, "Fundamental properties of surface waves in lossless stratified structures," *Proc. Roy. Soc. A, Math., Phys. Eng. Sci.*, vol. 466, no. 2120, pp. 2447–2469, Mar. 2010.

[18] F. Ghasemifard, M. Norgren, and O. Quevedo-Teruel, "Dispersion analysis of 2-D glide-symmetric corrugated metasurfaces using mode-matching technique," *IEEE Microw. Wireless Compon. Lett.*, vol. 28, no. 1, pp. 1–3, Jan. 2018.

[19] Q. Chen, F. Ghasemifard, G. Valerio, and O. Quevedo-Teruel, "Modeling and dispersion analysis of coaxial lines with higher symmetries," *IEEE Trans. Microw. Theory Techn.*, vol. 66, no. 10, pp. 4338–4345, Oct. 2018.

[20] B. A. Mouris, A. Fernandez-Prieto, R. Thobaben, J. Martel, F. Mesa, and O. Quevedo-Teruel, "On the increment of the bandwidth of mushroom-type EBG structures with glide symmetry," *IEEE Trans. Microw. Theory Tech.*, vol. 68, no. 4, pp. 1–11, Apr. 2020.

[21] N. Marcuvitz, *Waveguide Handbook*. New York, NY, USA: McGraw-Hill, 1951.

[22] A. A. Oliner and W. Rotman, "Periodic structures in trough waveguides," *Proc. IRE*, vol. 34, no. 1, pp. 134–142, 1956.

[23] S. Marini, Á. Coves, V. E. Boria, and B. Gimeno, "Efficient modal analysis of periodic structures loaded with arbitrarily shaped waveguides," *IEEE Trans. Microw. Theory Techn.*, vol. 58, no. 3, pp. 529–536, Mar. 2010.

[24] Á. Coves, S. Marini, B. Gimeno, and V. Boria, "Full-wave analysis of periodic dielectric frequency-selective surfaces under plane wave excitation," *IEEE Trans. Antennas Propag.*, vol. 60, no. 6, pp. 2760–2769, Jun. 2012.

[25] Y. Weitsch and T. F. Eibert, "Modal series expansion of eigensolutions for closed and open periodic waveguides," *IEEE Trans. Antennas Propag.*, vol. 60, no. 12, pp. 5881–5889, Dec. 2012.

[26] M. Bagheriasl, O. Quevedo-Teruel, and G. Valerio, "Bloch analysis of artificial lines and surfaces exhibiting glide symmetry," *IEEE Trans. Microw. Theory Techn.*, vol. 67, no. 7, pp. 2618–2628, Jul. 2019.

[27] F. Mesa, G. Valerio, R. Rodriguez-Berral, and O. Quevedo-Teruel, "Simulation-assisted efficient computation of the dispersion diagram of periodic structures," *IEEE Antennas Propag. Mag.*, early access, Aug. 26, 2020, doi: 10.1109/MAP.2020.3003210.

[28] M. Tsuji, S. Matsumoto, H. Shigesawa, and K. Takiyama, "Guided-wave experiments with dielectric waveguides having finite periodic corrugation," *IEEE Trans. Microw. Theory Techn.*, vol. MTT-31, no. 4, pp. 337–344, Apr. 1983.

[29] S. Amari, R. Vahldieck, J. Bornemann, and P. Leuchtmann, "Spectrum of corrugated and periodically loaded waveguides from classical matrix eigenvalues," *IEEE Trans. Microw. Theory Techn.*, vol. 48, no. 3, pp. 453–460, Mar. 2000.

[30] H. K. Liu and T. L. Dong, "Propagation characteristics for periodic waveguide based on generalized conservation of complex power technique," *IEEE Trans. Microw. Theory Techn.*, vol. 54, no. 9, pp. 3479–3485, Sep. 2006.

[31] F. Bongard, J. Perruisseau-Carrier, and J. R. Mosig, "Enhanced periodic structure analysis based on a multiconductor transmission line model and application to metamaterials," *IEEE Trans. Microw. Theory Techn.*, vol. 57, no. 11, pp. 2715–2726, Nov. 2009.

[32] R. Islam, M. Zedler, and G. V. Eleftheriades, "Modal analysis and wave propagation in finite 2D transmission-line metamaterials," *IEEE Trans. Antennas Propag.*, vol. 59, no. 5, pp. 1562–1570, May 2011.

[33] J. Naqui *et al.*, "Common-mode suppression in microstrip differential lines by means of complementary split ring resonators: Theory and applications," *IEEE Trans. Microw. Theory Techn.*, vol. 60, no. 10, pp. 3023–3034, Oct. 2012.

[34] N. W. Ashcroft and N. D. Mermin, *Solid State Physics*. Orlando, FL, USA: Harcourt, 1976.

[35] R. E. Collin, *Field Theory Guided Waves*, 2nd ed. New York, NY, USA: IEEE Press, 1990.

[36] J. D. Joannopoulos, S. G. Johnson, J. N. Winn, and R. D. Meade, *Photonic Crystals*, 2nd ed. Princeton, NY, USA: Princeton Univ. Press, 2007.

[37] D. M. Atkin, P. S. J. Russell, T. A. Birks, and P. J. Roberts, "Photonic band structure of guided bloch modes in high index films fully etched through with periodic microstructure," *J. Mod. Opt.*, vol. 43, no. 5, pp. 1035–1053, May 1996.

[38] A. Figotin and Y. A. Godin, "The computation of spectra of some 2D photonic crystals," *J. Comput. Phys.*, vol. 136, no. 2, pp. 585–598, Sep. 1997.

[39] A. P. Smith, N. W. Ashcroft, W. W. Ashcroft, and N. W. Ashcroft, "Rapid convergence of lattice sums and structural integrals in ordered and disordered systems," *Phys. B, Condens. Matter*, vol. 38, no. 18, pp. 12942–12947, 1988.

[40] D. Hermann, M. Frank, K. Busch, P. Wolfle, and P. Wölfle, "Photonic band structure computations," *Opt. Express*, vol. 8, no. 3, pp. 167–172, 2001.

[41] G. Valerio, P. Baccarelli, P. Burghignoli, and A. Galli, "Comparative analysis of acceleration techniques for 2-D and 3-D Green's functions in periodic structures along one and two directions," *IEEE Trans. Antennas Propag.*, vol. 55, no. 6, pp. 1630–1643, Jun. 2007.

[42] E. E. Hart, S. J. Cox, and K. Djidjeli, "Compact RBF meshless methods for photonic crystal modelling," *J. Comput. Phys.*, vol. 230, no. 12, pp. 4910–4921, Jun. 2011.

[43] F.-L. Li, Y.-S. Wang, and C. Zhang, "Boundary element method for bandgap computation of photonic crystals," *Opt. Commun.*, vol. 285, no. 5, pp. 527–532, Mar. 2012.

[44] L. Junyi and D. S. Balint, "An inverse method to determine the dispersion curves of periodic structures based on wave superposition," *J. Sound Vib.*, vol. 350, pp. 41–72, Aug. 2015.

[45] E. N. Bulgakov, D. N. Maksimov, P. N. Semina, and S. A. Skorobogatov, "Propagating bound states in the continuum in dielectric gratings," *J. Opt. Soc. Amer. B, Opt. Phys.*, vol. 35, no. 6, pp. 1218–1222, 2018.

[46] G. Valerio, S. Paulotto, P. Baccarelli, P. Burghignoli, and A. Galli, "Accurate bloch analysis of 1-D periodic lines through the simulation of truncated structures," *IEEE Trans. Antennas Propag.*, vol. 59, no. 6, pp. 2188–2195, Jun. 2011.

[47] F. Mesa, R. Rodríguez-Berral, and F. Medina, "On the computation of the dispersion diagram of symmetric one-dimensionally periodic structures," *Symmetry*, vol. 10, no. 8, p. 307, Aug. 2018.

[48] J. Shekel, "Matrix analysis of multi-terminal transducers," *Proc. IRE*, vol. 42, no. 5, pp. 840–847, May 1954.

[49] M. Bozzi, S. Germani, L. Minelli, L. Perregrini, and P. de Maagt, "Efficient calculation of the dispersion diagram of planar electromagnetic band-gap structures by the MoM/BI-RME method," *IEEE Trans. Antennas Propag.*, vol. 53, no. 1, pp. 29–35, Jan. 2005.

[50] T. Rozzi, L. Pierantoni, and M. Farina, "Eigenvalue approach to the efficient determination of the hybrid and complex spectrum of inhomogeneous, closed waveguide," *IEEE Trans. Microw. Theory Techn.*, vol. 45, no. 3, pp. 345–353, Mar. 1997.

[51] P. J. B. Clarricoats and K. R. Slinn, "Complex modes of propagation in dielectric-loaded circular waveguides," *Electron. Lett.*, vol. 1, no. 5, pp. 145–146, Jul. 1965.

[52] A. S. Omar and K. F. Schunemann, "Complex and backward-wave modes in inhomogeneously and anisotropically filled waveguides," *IEEE Trans. Microw. Theory Techn.*, vol. MTT-35, no. 3, pp. 268–275, Mar. 1987.
[53] M. J. Freire, F. Mesa, and M. Horno, "Excitation of complex and backward mode on shielded lossless printed lines," *IEEE Trans. Microw. Theory Techn.*, vol. 47, no. 7, pp. 1098–1105, Jul. 1999.
[54] A. L. Fructos, S. Campione, F. Capolino, and F. Mesa, "Characterization of complex plasmonic modes in two-dimensional periodic arrays of metal nanospheres," *J. Opt. Soc. Amer. B, Opt. Phys.*, vol. 28, no. 6, pp. 1446–1458, 2011.
[55] R. Marques, F. L. Mesa, and M. Horno, "Nonreciprocal and reciprocal complex and backward waves in parallel plate waveguides loaded with a ferrite slab arbitrarily magnetized," *IEEE Trans. Microw. Theory Techn.*, vol. 41, no. 8, pp. 1409–1418, Mar. 1993.
[56] W.-Y. He and C. T. Chan, "The emergence of dirac points in photonic crystals with mirror symmetry," *Sci. Rep.*, vol. 5, no. 1, p. 8186, Feb. 2015.
[57] L. P. Castro, R. Duduchava, and D. Kapanadze, "Electromagnetic scattering by cylindrical orthotropic waveguide irises," *Georg. Math. J.*, vol. 18, no. 1, pp. 99–120, 2011.
[58] Y. F. Wang, Y. S. Wang, and C. Zhang, "Bandgaps and directional properties of two-dimensional square beam-like zigzag lattices," *AIP Adv.*, vol. 4, no. 12, pp. 124403-1–124403-12, 2014.
[59] Y.-F. Wang, Y.-S. Wang, and C. Zhang, "Bandgaps and directional propagation of elastic waves in 2D square zigzag lattice structures," *J. Phys. D, Appl. Phys.*, vol. 47, no. 48, Nov. 2014, Art. no. 485102.
[60] Z.-G. Chen, J. Zhao, J. Mei, and Y. Wu, "Acoustic frequency filter based on anisotropic topological phononic crystals," *Sci. Rep.*, vol. 7, no. 1, pp. 1–6, Dec. 2017.
[61] P.-S. Kildal, E. Alfonso, A. Valero-Nogueira, and E. Rajo-Iglesias, "Local metamaterial-based waveguides in gaps between parallel metal plates," *IEEE Antennas Wireless Propag. Lett.*, vol. 8, pp. 84–87, Dec. 2009.

Qiao Chen (Member, IEEE) was born in Nanjing, China, in November 1990. He received the B.Sc. degree in information engineering and the M.Sc. and Ph.D. degrees in electromagnetic and microwave engineering from Southeast University, Nanjing, China, in 2013, 2015, and 2020, respectively.

From 2017 to 2019, he was with a Joint-Ph.D. Program, Division of Electromagnetic Engineering, KTH Royal Institute of Technology, Stockholm, Sweden, where he is currently working as a Post-Doctoral Researcher. His research interests include leaky-wave antennas, lens antennas, metasurfaces, array antennas, higher symmetric periodic structures, and microwave circuits and systems.

Francisco Mesa (Fellow, IEEE) received the Licenciado and Ph.D. degrees in physics from the Universidad de Sevilla, Seville, Spain, in 1989 and 1991, respectively.

He is currently a Professor with the Departamento de Física Aplicada 1, Universidad de Sevilla. His research interest includes electromagnetic propagation/radiation in planar structures.

Xiaoxing Yin (Member, IEEE) was born in Taiyuan, China. He received the B.Sc. degree in radio engineering and the M.Sc. and Ph.D. degrees in electronic engineering from Southeast University, Nanjing, China, in 1983, 1989, and 2001, respectively.

From 1983 to 1986 and 1989 to 1998, he was with the Department of Physics, University of Petroleum, Dongying, China, where he was involved in logging methods and instruments. Since 2001, he has been a Lecturer with the State Key Laboratory of Millimeter Waves, Southeast University, where he is currently a Professor. He has authored or coauthored 63 technical articles. He holds over 30 patents. His current research interests include computational electromagnetics, microwave components and system, and antennas.

Oscar Quevedo-Teruel (Senior Member, IEEE) received the degree in telecommunication engineering from the Carlos III University of Madrid, Madrid, Spain, in 2005, part of which was done at the Chalmers University of Technology in Gothenburg, Gothenburg, Sweden, and the Ph.D. degree from the Carlos III University of Madrid, in 2010.

He was a guest Post-Doctoral Researcher with the University of Delft, Delft, The Netherlands. From 2010 to 2011, he joined the Department of Theoretical Physics of Condensed Matter, Universidad Autonoma de Madrid, as a Research Fellow and then as a Post-Doctoral Researcher with the Queen Mary University of London, London, U.K., from 2011 to 2013. In 2014, he joined the Division for Electromagnetic Engineering, School of Electrical Engineering and Computer Science, KTH Royal Institute of Technology, Stockholm, Sweden, where he is currently an Associate Professor and the Director of the Master Program in Electromagnetics Fusion and Space Engineering. He has made scientific contributions to higher symmetries, transformation optics, lens antennas, metasurfaces, leaky wave antennas, multimode microstrip patch antennas, and high impedance surfaces. He is the coauthor of 93 articles in international journals and 140 at international conferences.

Dr. Quevedo-Teruel was the EurAAP Delegate for Sweden, Norway, and Iceland from 2018 to 2020 and he has been a member of the EurAAP Board of Directors since January 2021. He is a Distinguished Lecturer of the IEEE Antennas and Propagation Society from 2019 to 2021. He has been an Associate Editor of the IEEE TRANSACTIONS ON ANTENNAS AND PROPAGATION since 2018 and has been the Founder and Editor-In-Chief of the *EurAAP* Journal *Reviews of Electromagnetics* since 2020.